ACS APPLIED ENERGY MATERIALS

www.acsaem.org Article

Bonding Heterogeneity Inducing Low Lattice Thermal Conductivity and High Thermoelectric Performance in 2D $CdTe_2$

Biao Wan, Zhibin Gao, Xiaochen Huang, Yuqian Yang, Liangchao Chen, Qianqian Wang, Chao Fang, Weixia Shen, Yuewen Zhang, Hongan Ma, Huiyang Gou, Xiaopeng Jia, and Zhuangfei Zhang*

Cite This: *ACS Appl. Energy Mater.* 2022, 5, 9549−9558 Read Online

ACCESS | Metrics & More | Article Recommendations | Supporting Information

ABSTRACT: Two-dimensional (2D) materials have emerged as a broad platform for exploring promising thermoelectric materials. Motivated by the fabrication of diverse artificially designed Te-based 2D materials with high thermoelectric performance, here, we predicted 2D hexagonal CdTe and pentagonal $CdTe_2$ for potential thermoelectric materials, using the particle swarm optimization (PSO) method combined with density functional theory. CdTe and $CdTe_2$ show predicted direct/indirect band gaps of 1.82 and 1.96 eV, respectively. Chemical bonding analysis revealed that all the Te atoms in CdTe are coupled through uniform ionic bonding. $CdTe_2$ exhibits bonding heterogeneity, arising from weak the Cd−Te ionic bonding and strong Te−Te covalent bonding. Based on Boltzmann transport theory, we found that the bonding heterogeneity in $CdTe_2$ favors low lattice conductivity. The calculated lattice thermal conductivity of $CdTe_2$ is 0.33 Wm^{-1} K^{-1} at 300 K, which was contributed by the weaker coupling between acoustic and optical phonon modes, low group velocities of the acoustic modes, and high lattice anharmonicity. On the other hand, the occupied π^*_{5p}, π_{5p}, and σ_{5p} bondings in Te−Te pairs significantly facilitate the electrical conductivity and enhance the Seebeck coefficient of p-type $CdTe_2$. The low thermal conductivity and high power factor in $CdTe_2$ give rise to a high thermoelectric performance at low temperature. Our findings should encourage the exploration of 2D materials for thermoelectric applications with strong bonding heterogeneity.

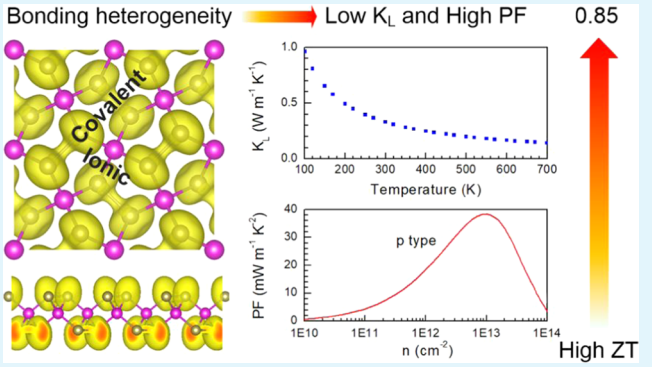

KEYWORDS: *two-dimensional material, ab initio calculations, thermoelectric property, crystal structure prediction, bonding heterogeneity*

INTRODUCTION

The extensive combustion of fossil fuels has induced serious global warming and environmental pollution. Consequently, it is urgent to develop new economical and environmentally friendly energy sources to reduce the emission of greenhouse gases. As an alternative approach, thermoelectric (TE) materials have drawn wide interests recently, which can directly convert waste thermal energy into electricity.[1,2] The efficiency of thermoelectric materials can be evaluated by the figure of merit (*zit*), $zT = S^2\sigma T/\kappa$,[3,4] where S is the Seebeck coefficient, σ is the electrical conductivity, and κ is thermal conductivity, which was contributed by electrical (κ_e) and lattice thermal conductivities (κ_L). Thus, the simultaneous presence of large S and σ coupled with low κ can lead to a high zT. However, the S and σ are usually interwoven and show an opposite trend, which induces the power factor (PF) PF = $S^2\sigma$ hard to improve. In the past few decades, extensive studies were performed to improve the low PF, such as band structure engineering by tuning the composition or doping heteroatoms[5−7] and searching new materials with multivalley bands or combination of flat and dispersive bands around the Fermi level.[8−10] For semiconductors, the thermal conductivity is dominantly controlled by the phonon transport property. Thus, a reduced κ_L can effectively improve thermoelectric performance. Defect engineering or nanostructuring is usually used to increase phonon scattering, inducing low thermal transport properties.[11−13] However, these strategies sometimes lead to a degradation of the electronic transport properties. Thus, exploring compounds with intrinsic low κ_L has been of great interest because the electronic transport properties can be optimized with a small effect on the κ_L. Compounds with high atomic mass usually lead to low κ_L. The bonding hierarchy,[14] weak bonding,[15] and resonant bonding[16] also can significantly suppress the transport of phonons. Moreover, the bonding heterogeneity in Cu_3SbSe_3,[17] $CsAg_5Te_3$,[18] and $BaAgYTe_3$[19] was observed to induce rattle-like vibrations and

Received: April 19, 2022
Accepted: July 14, 2022
Published: July 26, 2022

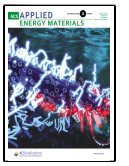

https://doi.org/10.1021/acsaem.2c01176
ACS Appl. Energy Mater. 2022, 5, 9549−9558

high lattice anharmonicity, leading to an ultralow lattice conductivity and high *zit*.

Two-dimensional (2D) materials are promising candidates for thermoelectric materials because of the quantum confinement effect, which can break the interwoven relation between S and σ.[20] Diverse advanced 2D thermoelectric materials with low κ_L and high electronic transport properties have been reported in recent years, such as the 2D pentagonal TMM_2 (TM = Pd, Pt; M = S, Se, Te),[21,22] triphosphides (e.g., In P_3, GaP_3 and SnP_3),[23,24] transition metal chalcogenides M_2X (M = metal and X = O, S, Se and Te),[25−28] SnSe,[29] and InSe.[30] Among them, the 2D Te-based materials have attracted tremendous interest due to the heavy atomic mass, which can suppress the transport of phonons. In 2018, Liu et al.[31] fabricated a hexagonal monolayer $PdTe_2$ with superconducting behavior. Afterward, a theoretical study by Marfoua et al. reported the hexagonal and pentagonal $PdTe_2$ with zT = 0.8 at 300 K, using the Boltzmann transport equation.[32] A similar phenomenon was also observed in 2D $PtTe_2$.[22] Other 2D Te-based materials such as the group IIIA/IVA-Te (e.g., InTe,[33] SnTe,[34] and GaTe[35]) have also been extensively investigated as promising thermoelectric materials. Bulk CdTe[36] and $CdTe_2$[37] are semiconductors with band gaps of 1.50 (direct) and 1.08 eV (indirect), respectively. CdTe thin films have been widely used in solar cell prototyping.[38] In 2017, researchers predicted a α-CdTe (tetragonal-PbO structure) monolayer with low formation enthalpy and excellent dynamic stability. The novel electronic structure endows 2D α-CdTe with a promising application potential in optoelectronic devices.[39] In 2020, Naseri et al. built a planar 2D CdTe, with the use of the predicted CdS honeycomb structure.[40] Afterward, Kolobov et al. reported a two-monolayer-thick CdTe slab (cleaved from bulk CdTe) that has extremely low formation enthalpies and a direct band gap of 1.03 eV.[41] However, the structure configuration, phase stability, and thermoelectric performance of diverse 2D CdTe still lack a full investigation.

In this work, we carried out extensive structural searches to explore 2D CdTe materials (i.e., CdTe, $CdTe_2$, and $CdTe_3$), using the particle swarm optimization (PSO) method. 2D CdTe and $CdTe_2$ were verified to be stable 2D materials with low formation enthalpies and excellent dynamic stability. Through bonding analysis, $CdTe_2$ exhibits strong bonding heterogeneity, originating from weak Cd−Te ionic bonding and strong Te−Te covalent bonding. The loosely bound Cd atoms and quasi-sandwich structure in $CdTe_2$ give rise to low group velocities of the acoustic modes. The bonding heterogeneity in $CdTe_2$ introduces lattice anharmonicity, which is manifested in the larger mode Grüneisen parameters. Moreover, the different bonding strengths render $CdTe_2$ quite localized optical phonons with low frequency, leading to weaker coupling between acoustic and optical phonon modes, which can significantly suppress the transport of phonons. On the other hand, the occupied π^*_{5p}, π_{5p}, and σ_{5p} bondings in covalent Te−Te pairs give rise to a superior p-type electronic conductivity and high Seebeck coefficient of p-type $CdTe_2$, making it a promising thermoelectric material at room temperature.

■ COMPUTATIONAL APPROACH

The structural searches of 2D CdTe, $CdTe_2$ and $CdTe_3$ were carried out in crystal structure analysis by particle swarm optimization (CALYPSO) methodology,[42,43] whose validity has been verified by correctly predicting many bulk and 2D materials.[44,45] In the structural search process, 40 generations were searched, each generation containing 40 structures. The chemical formula of the generated CdTe structures was set as 1−8. Beyond the structural searches, the frequently reported 2D crystal structures, such as InP_3[23] and penta-$PdTe_2$,[21] were also considered. However, the 2D CdTe with the structure prototypes was significantly distorted after full structure relaxation. *Ab initio* calculations were performed in the Vienna Ab Initio Simulation Package (VASP) code.[46] The electron−ion interaction was described using the projector augmented wave potential (PAW) method and applying the Perdew−Burke−Ernzerhof (PBE) exchange−correlation functional.[47,48] To ensure that all the enthalpy calculations were well converged to 1 meV/atom, the kinetic energy cutoff was set at 500 eV. Also, 11 × 11 × 1 and 7 × 7 × 1 Monkhorst−Pack k-point meshes were used for 2D CdTe and $CdTe_2$, respectively. Since the 2D Te has been experimentally synthesized,[49] we select bulk Cd and the most stable 2D Te (α-Te)[50] as references to calculate the formation enthalpies and access the experimental feasibility.

$$\Delta H(\mathrm{CdTe}_x) = \frac{[H(\mathrm{CdTe}_x) - H(\mathrm{Cd}) - xH(\mathrm{Te})]}{1 + x} \quad (1)$$

where H denotes the enthalpy per chemical unit for $CdTe_x$, Cd, and Te. The Heyd−Scuseria−Ernzerhof (HSE06) exchange−correlation functional was used to calculate the electronic band structures.[51] The band structure with the HSE06 + SOC correction was calculated separately and is plotted in Figure S1. Since the HSE06+SOC correction is much time-consuming, we only consider the HSE06 correction in our article. Considering that the density functional theory calculations were performed at 0 K, *ab initio* molecular dynamics (AIMD) simulations were done at 300 K to evaluate the thermal stability of 2D CdTe at room temperature. A canonical ensemble (NVT) with a Nóse-Hoover heat bath scheme was used,[52] and 20,000 steps were calculated with a time step of 2 fs. To minimize the constraint induced by periodicity, the lattice vector of CdTe was converted to a rectangle, and then, a 5 × 5 × 1 supercell (100 atoms) was created, while for the 2D $CdTe_2$, a 4 × 4 × 1 supercell (96 atoms) was created. The crystal orbital Hamiltonian population (COHP) analyses were performed using the LOBSTER code to uncover the bonding characters of CdTe and Te−Te pairs.[53]

The electronic transport properties of S, σ, and κ_e were calculated using semiclassical Boltzmann theory within the constant scattering time approximation using the BoltzTraP code.[54,55] The reliability of this method has been verified by many studies.[22,50] Denser 25 × 25 × 1 and 20 × 20 × 1 k-point meshes were used for 2D CdTe and $CdTe_2$, respectively. The κ_L was calculated based on the phonon Boltzmann transport equation, as implemented in the ShengBTE code.[56] Phonon dispersions and second-order interatomic force constants (2nd IFCs) were calculated using Phonopy packages[57] with a supercell of 5 × 5 × 1 both for 2D CdTe and $CdTe_2$. The third-order interatomic force constants (3^{rd} IFCs) were calculated using the same supercell. The cutoff radius was set to 5.53 Å (up to the fifth nearest neighbors) for CdTe and 6.38 Å (up to the fifth nearest neighbors) for $CdTe_2$, under the consideration of accuracy and cost. The κ_L convergence test is shown in Figure S2. A dense phonon q-grid of 101 × 101 × 1 was used to calculate the κ_L of 2D CdTe and $CdTe_2$. During the electronic and thermal property calculations, the effective

https://doi.org/10.1021/acsaem.2c01176
ACS Appl. Energy Mater. 2022, 5, 9549−9558

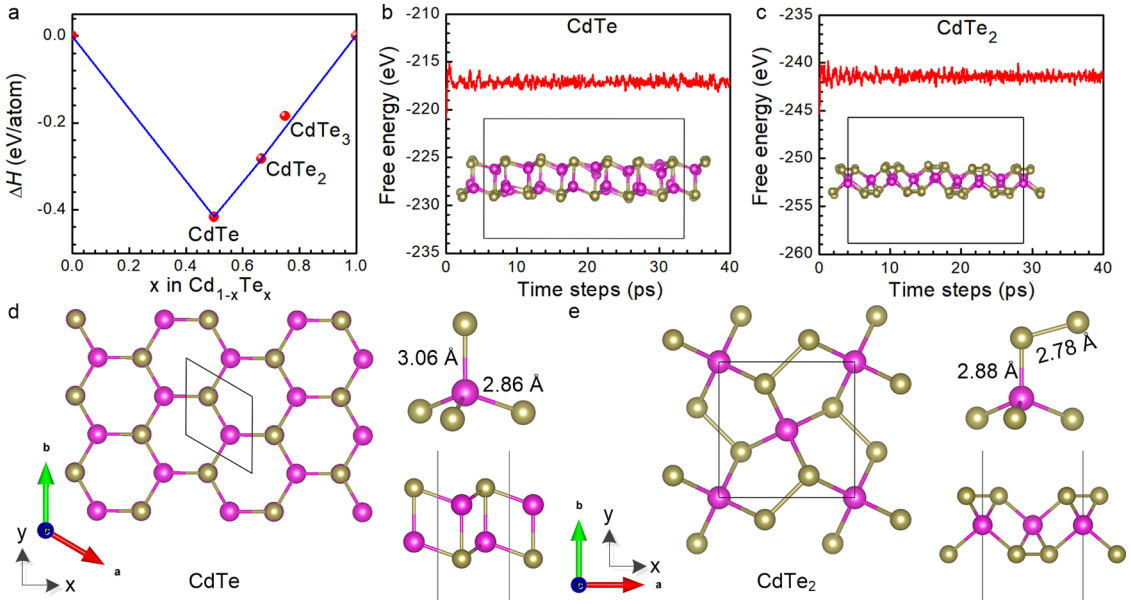

Figure 1. Convex hull for 2D CdTe (a). MD simulations at 300 K for CdTe (b) and $CdTe_2$ (c); insets are the crystal structures for CdTe and $CdTe_2$ after the 40 ps simulation. Crystal structures of CdTe (d) and $CdTe_2$ (e).

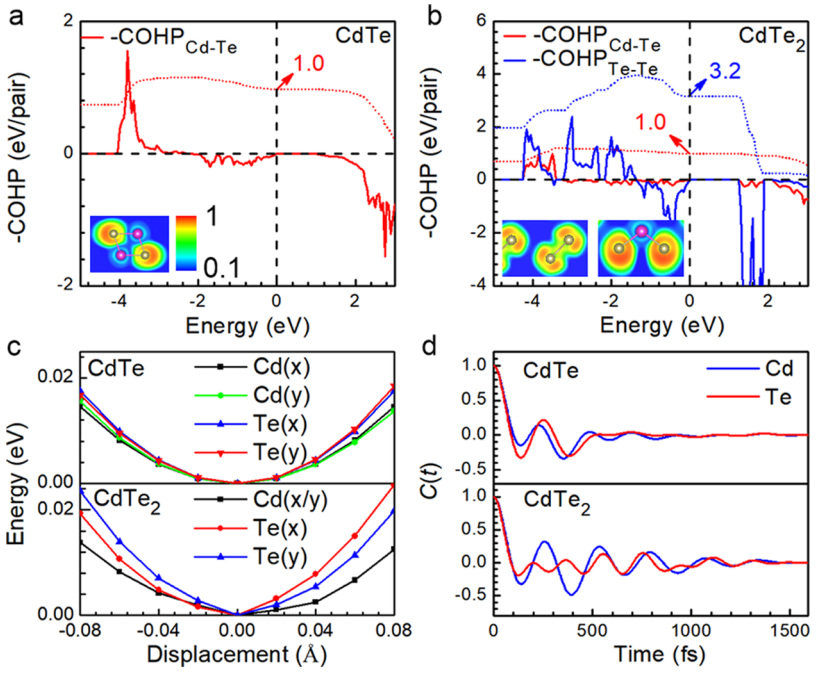

Figure 2. Calculated −COHP and −ICOHP (dashed line) curves for 2D CdTe (a) and $CdTe_2$ (b), insets are the ELF maps, and brown and pink spheres represent Te and Cd atoms, respectively. Potential energy well of Cd and Te atoms as a function of displacements along the *x* or *y* axis of the 2D CdTe (c). Velocity autocorrelation function (VACF) of Cd and Te atoms in 2D CdTe (d).

thicknesses for the CdTe and $CdTe_2$ were considered to be 8.13 and 7.64 Å, respectively.

RESULTS AND DISCUSSION

Structure and Phase Stability. Extensive unbiased structure searches were carried out for CdTe, $CdTe_2$, and $CdTe_3$. To access the experimental feasibility, the phase stability of most stable 2D CdTe materials was verified by the calculation of formation enthalpies (ΔH) with the use of bulk Cd and the most stable 2D Te (α-Te)[50] as references. The calculated formation enthalpies of CdTe, $CdTe_2$, and $CdTe_3$ are −0.417, −0.283, and −0.185 eV/atom, respectively. Based on the formation enthalpies, we constructed the convex hull. As shown in Figure 1a, phases on the convex hull are stable against decomposing into the nearest compositions. Both the 2D CdTe and $CdTe_2$ are on the convex hull; however, the $CdTe_3$ is above the convex hull and can decompose into $CdTe_2$ and Te monolayers. Thus, we only discuss the 2D CdTe and $CdTe_2$ in the following section. Considering that the calculations were carried out at 0 K, we performed the AIMD simulations at 300 K for 2D CdTe (Figure 1b) and $CdTe_2$ (Figure 1c). During the AIMD simulations, the total energy is nearly constant. After a 40 ps simulation, the crystal

https://doi.org/10.1021/acsaem.2c01176
ACS Appl. Energy Mater. 2022, 5, 9549−9558

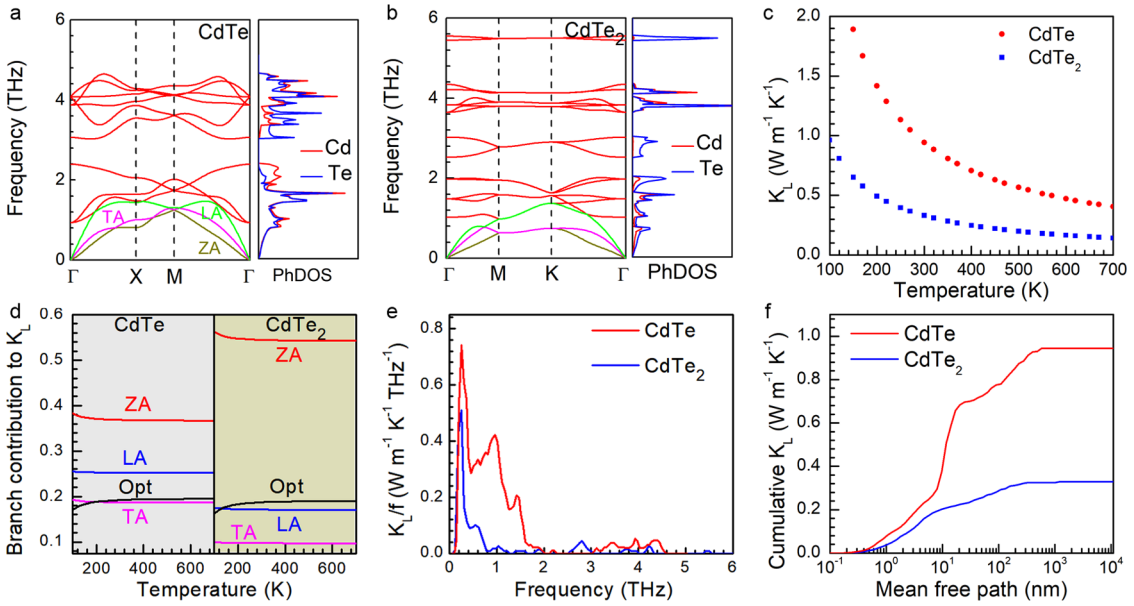

Figure 3. Phonon dispersion and phonon density of states of CdTe (a) and $CdTe_2$ (b). Lattice thermal conductivity κ_L as a function of temperature (c). Branch contribution to κ_L as a function of temperature (d). Frequency-resolved κ_L at 300 K (e). Cumulative κ_L as a function of the phonon mean free path at 300 K (f).

structures of CdTe and $CdTe_2$ monolayers remained intact, suggesting that both the 2D CdTe and $CdTe_2$ are stable at ambient temperature.

Detailed top and side views of CdTe and $CdTe_2$ monolayer structures are shown in Figure 1d,e, respectively. Other metastable 2D CdTe, $CdTe_2$, and $CdTe_3$ are shown in Figure S3. Consistent with the investigation of Kolobov et al.,[41] the CdTe monolayer adopts a honeycomb prototype with the space group $P\bar{3}m1$ and lattice constants $a = b = 4.67$ Å. In CdTe, each Cd atom is coordinated by four Te atoms in CdTe with two distinct distances of 2.86 and 3.06 Å. The $CdTe_2$ adopts a typical penta-structure with the symmetry group $P\bar{4}2_1m$ and lattice constants $a = b = 6.06$ Å. Unlike the 2D $PdTe_2$[21] and $PtTe_2$[22] penta-structures, the $CdTe_2$ adopts a quasi-sandwich structure with Te−Cd−Te stacking. Similar to CdTe, all the Cd atoms are coordinated by four Te atoms with a uniform distance, 2.88 Å. The Cd−Te distances in both CdTe and $CdTe_2$ are comparable to those of bulk CdTe (2.86 Å). Considering the large electronegativity difference, it can be speculated that the Cd−Te bonding is coupled primarily through ionic bonding. The higher Te concentration in 2D $CdTe_2$ induced the nearest Te atoms to form Te−Te dimers with a short distance of 2.78 Å, which is shorter than that of 2D α-Te (3.04 Å),[50] indicating a strong covalent bonding character. The detailed atom positions are listed in Table S1.

Bonding Analysis. To unambiguously reveal the bonding character of the Cd−Te and Te−Te pairs, we calculated the crystal orbital Hamilton population (COHP, −COHP plotted here) curves for 2D CdTe (Figure 2a) and $CdTe_2$ (Figure 2b). COHP is an efficient way to investigate bonding characters, which partitions the band structure energy into orbital pair interactions, and stronger bonding can lead to higher −COHP peaks. As shown in Figure 2a,b, Te−Te pairs exhibit much higher −COHP curves than Cd−Te pairs in both 2D CdTe and $CdTe_2$, suggesting a stronger bonding strength in Te−Te pairs. The −COHP integration (−ICOHP, dashed line in Figure 2a,b) at the Fermi level can quantitatively determine the bonding strength; Cd−Te pairs have low −ICOHP values of 1.0 eV/pair both in CdTe and $CdTe_2$, while the −ICOHP for Te−Te pairs in $CdTe_2$ is 3.16 eV/pair, confirming their much stronger bonding strength and a potential covalent bonding character. The inserts in the figure are the electron localization function (ELF)[58] maps around Cd−Te and Te−Te pairs. The ELF between Cd and Te atoms is nearly zero both in CdTe and $CdTe_2$, revealing the ionic bonding nature. High ELF values (approximately 0.76) can be observed in the Te dimers, suggesting a strong covalent bonding character. Noteworthily, the negative −COHP values within −1.6 and 0.0 eV represent that strong antibonding states exist in Te−Te pairs. Such antibonding states originated from the π^* bonding of p orbitals, which have also been observed in other chalcogenides, e.g., Na_2S_3[45] and Ag_xTe_{1-x}.[59] Considering the atomic arrangement of Cd and Te atoms, $CdTe_2$ can be viewed as a quasi-bonding hierarchy structure with covalent−ionic−covalent stacking.

To investigate the influence of bonding heterogeneity on the atomic-level dynamics of $CdTe_2$, we calculated the potential energy curves of Cd and Te atoms by displacing them along x/y directions from their equilibrium positions (Figure 2c). In the 2D CdTe, the Cd and Te atoms are located in similar potential wells caused by the uniform ionic bonding. In the $CdTe_2$, Cd atoms lay in shallower potential wells compared with CdTe, whereas Te atoms lay in much deeper energy wells. This showed that the Cd atoms in $CdTe_2$ can vibrate more easily than in CdTe, and the vibrations of the Te atoms are damped in $CdTe_2$. This phenomenon was also verified by the velocity autocorrelation function (VACF).[60,61] As shown in Figure 2d, the oscillations of Cd and Te atoms are similar in CdTe but sharply different in $CdTe_2$. In $CdTe_2$, the oscillations of Cd atoms are more substantial than those of CdTe; however, the Te atoms are damped significantly, confirming the strong chemical bonding heterogeneity in $CdTe_2$. Similar with $Cu_{12}Sb_4S_{13}$[62] and $BaAgYTe_3$,[19] the bonding heterogeneity in $CdTe_2$ may significantly enhance the scattering of the heat-carrying phonon and suppress the lattice thermal conductivity.

https://doi.org/10.1021/acsaem.2c01176
ACS Appl. Energy Mater. 2022, 5, 9549−9558

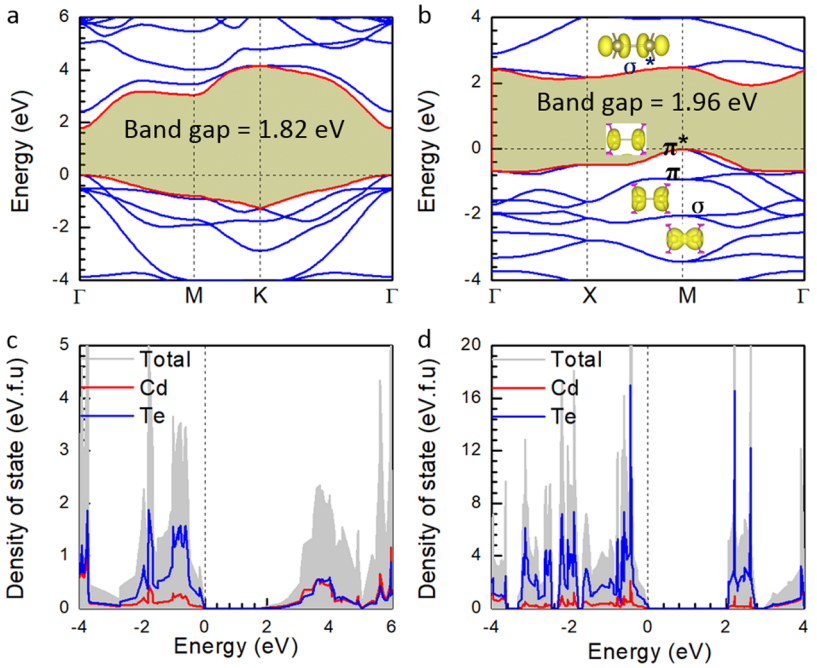

Figure 4. Band structure for CdTe (a) and $CdTe_2$ (b) monolayers. Total and partial density of states for CdTe (c) and $CdTe_2$ (d). Insets are the partial charge density of the valence band in the $CdTe_2$ monolayer.

Lattice Thermal Conductivity. Phonon dispersion analyses can effectively assess the κ_L. Thus, we calculated the phonon dispersion for CdTe (Figure 3a) and $CdTe_2$ (Figure 3b). The three acoustic phonon branches which correspond to an out-of-plane flexural acoustic mode, an in-plane transverse acoustic mode, and an in-plane longitudinal acoustic mode are marked as ZA, TA, and LA, respectively. There is no negative frequency observed in the entire Brillouin zone for either CdTe or $CdTe_2$, confirming their dynamic stability. Generally, higher cutoff frequencies of an acoustic branch can lead to higher κ_L. Both the CdTe and $CdTe_2$ monolayers show low cutoff frequencies of ZA, TA, and LA branches, i.e., 1.23, 1.29, and 1.46 THz in CdTe and 0.76, 0.78, and 1.36 THz in $CdTe_2$, respectively, which are comparable to those of 2D Cu_2S[25] and InP_3.[24] Such low acoustic branch frequencies are dominantly contributed by the high atomic mass of Cd and Te atoms. Moreover, there is no phonon gap between acoustic and optical branches in either CdTe or $CdTe_2$, suggesting a strong optical−acoustic phonon scattering, which can further suppress the κ_L.[50]

Notably, the $CdTe_2$ possesses much lower cutoff frequencies of acoustic branches, contributed by the loosely bound Cd atoms and the quasi-sandwich structure with covalent−ionic−covalent stacking, which is similar to that of $BaAu_2P_4$[14] and AgBiTeO[63] with bonding hierarchy. As shown in Figure S4, compared with CdTe, the lower cutoff frequencies of acoustic branches induced small group velocities in $CdTe_2$. The relatively larger mode Grüneisen parameters of acoustic branches in $CdTe_2$ suggested that the bonding heterogeneity induced larger lattice anharmonicity. Moreover, there is one phonon gap in the optical branches of CdTe, located at around 2.4 THz, whereas five gaps exist in $CdTe_2$, located at around 1.5, 2.0, 3.0, 4.0, and 4.3 THz. We calculated the phonon DOS to uncover such a phenomenon (Figure 3a,b). The Cd and Te atoms are strongly hybridized both in CdTe and $CdTe_2$, which arises from their similar atomic mass values. For $CdTe_2$, strong covalent bonding in Te−Te pairs leading to stiffer elastic constants and higher frequencies of optical branches gives rise to a weaker hybridization, quasi-localized phonon branches, and multiple gaps in optical branches. These localized optical phonons with low frequencies induce multiple scattering channels, which can significantly suppress the transport of phonons.[19] Moreover, the higher frequencies of optical branches in $CdTe_2$ give rise to a weaker coupling between acoustic and optical phonon modes, indicating a higher optical−acoustic phonon scattering and leading to a lower κ_L.

The κ_L values of CdTe and $CdTe_2$ were obtained from the iterative solution of the linearized Boltzmann transport equation. The calculated κ_L values for CdTe and $CdTe_2$ in the range of 300−700 K are plotted in Figure 3c. The κ_L decreased with increasing temperature. Both the CdTe and $CdTe_2$ monolayers exhibit an ultralow κ_L at 300 K, 0.94 and 0.33 $Wm^{-1} K^{-1}$, respectively, much lower than that of 2D α-Te (9.85 $Wm^{-1} K^{-1}$ at 300 K)[50] and comparable to that of In_2S_3-doped Cu_2S (0.95 $Wm^{-1} K^{-1}$ at 850 K).[64] Consistent with the chemical bonding and phonon dispersion analysis, the κ_L of $CdTe_2$ is almost half as large as that of CdTe in the entire temperature range. Thus, bonding heterogeneity induced by the coexistence of ionic and covalent bondings can significantly suppress the κ_L. These phenomena were further clarified, and the influence of the Te concentration was excluded, by reviewing the previously reported 2D $PdTe_2$.[32] The κ_L of P-$PdTe_2$ with the coexistence of Pd−Te and Te−Te bonding is almost half as large as that of H-$PdTe_2$ with uniform Pd−Te bonding.[32]

The normalized contributions of acoustic and optical branches to κ_L are shown in Figure 3d. The contribution of ZA branches dominates the κ_L in both CdTe and $CdTe_2$ monolayers. The proportions of contributions of ZA, TA, LA, and optical branches to the total κ_L are 36.7, 18.6, 25.2, and 19.5%, respectively, in CdTe and 54.2, 9.7, 17.1, and 19.0%, respectively, in $CdTe_2$. Consistently, the frequency-resolved κ_L at 300 K in CdTe (Figure 3e) shows that phonons with frequencies lower than 1.8 THz are the primary contributors to

https://doi.org/10.1021/acsaem.2c01176
ACS Appl. Energy Mater. 2022, 5, 9549−9558

total κ_L, whereas the optical branches with high frequencies show small contributions. For $CdTe_2$, the main contribution to κ_L comes from ZA branches with frequencies lower than 0.8 THz and the optical branch with frequencies around 3Hz (originating from Te atoms as shown in Figure 3b).

The κ_L as a function of the phonon mean free path (MFP) is an important parameter to estimate the size effects and design nanostructures with optimized κ_L.[11,65] As shown in Figure 3f, almost all phonons have an MFP below 1 μm in 2D CdTe. Notably, phonons in CdTe with MFPs below 20 nm contribute 3/4 of the κ_L, implying that the κ_L of CdTe can decrease sharply with a sample of less than 20 nm.

Electronic Structure. The band structure and density of states (DOS) were calculated using the HSE06 hybrid functional. The 2D CdTe possesses a direct band gap of 1.82 eV with the valence band maximum (VBM) and conduction band minimum (CBM) located at Γ points. Our predicted band gap is higher than the previously reported value (1.03 eV), obtained using the PBEsol method.[41] The highly dispersive CBM and relatively flat VBM in CdTe suggest a low electronic and high hole effective mass. Similar to the pentagonal PtS_2,[66] the 2D $CdTe_2$ has an indirect band gap of 1.96 eV with the VBM located at M points and the CBM located between M and Γ points. In $CdTe_2$, both the CBM and VBM are highly dispersive, indicating a low electron and hole effective mass. Moreover, the valence bands are localized and highly degenerate around the Fermi level, which can significantly enhance the electrical conductivity and Seebeck coefficient, resulting in a high thermoelectric power factor.[67] To investigate the origin of such degenerated valence bands, we calculated the partial charge densities of these bands. As shown in the inset of Figure 4d, based on the partial charge density and COHP analyses (Figure 2b), these degenerated valence bands originate from the strong covalent Te−Te π^* bonding. Furthermore, the π and σ bondings formed by Te-5p orbitals are also distributed around the Fermi level, whereas the unoccupied σ^* bonding dominantly contributes to the conduction bands. Thus, the Te−Te covalent bonding induced a high DOS with sharp peaks around the Fermi level, which can significantly enhance the power factor of p-type $CdTe_2$.

Electronic Transport Coefficients. To explore the electronic transport coefficients of the CdTe and $CdTe_2$ monolayers, we first explore the relaxation time τ, which is proportional to the electronic conductivity. The relaxation time τ was calculated through the well-known model

$$\tau = \frac{m^*\mu}{e} \tag{2}$$

where m^* is the effective mass of electrons and holes, μ is the carrier mobility, and e is the electron charge. For 2D materials, the μ can be derived using Bardeen−Shockley deformation potential (DP) theory,[68] given by

$$\mu_{2D} = \frac{2e\hbar^3 C_{2D}}{3\kappa_B T m^{*2} E_d^2} \tag{3}$$

where $\hbar$ is the reduced Planck constant, C_{2D} is the two-dimensional elastic modulus, which can be calculated through applying stress under uniaxial strain, k_B is the Boltzmann constant, T is the temperature (in K), and E_d is the deformation potential, which can be calculated by

$$E_d = \frac{\partial E_{edge}}{\partial l / l_0} \tag{4}$$

where E_{edge} is the maximum (minimum) energy value of the VBM (CBM) under small compression and expansion, l_0 is the lattice parameter, and ∂l is the variation of the lattice parameter. The energy of core electrons is considered as the energy reference.

Table 1 lists the calculated carrier mobilities and relaxation time for electrons and holes for CdTe and $CdTe_2$. Consistent with the bonding and electronic structure analysis, p-type $CdTe_2$ shows superior carrier mobility. The strong anisotropy in $CdTe_2$ was also observed in pentagonal PtM_2 (M = S, Se, Te),[22] ZrS_3,[69] and As_2Te_3.[70]

Table 1. Calculated DP Constant E_d (eV), Elastic Modulus C_{2D} (N m^{-1}), Effective Mass m^* (m^*/m_0), Carrier Mobility μ (cm^{2}V^{-1}s^{-1}), and Relaxation Time τ (ps) at 300 K for CdTe and $CdTe_2$ monolayers

phase	carrier type	E_d	C_{2D}	m^*	μ	τ
CdTe	electron	13.44	99.10	0.12	542.13	0.04
	hole	4.65		1.00	66.21	0.04
$CdTe_2$	electron	8.85	39.20	0.61	19.52	0.01
	hole	1.47		0.37	1929.57	0.40

Boltzmann transport theory (BTE) was used to evaluate σ, S, and κ_e. The Seebeck coefficients and electrical conductivities of CdTe and $CdTe_2$ as a function of the carrier concentration at 300, 500, and 700 K are shown in Figure 5a,b,d,e. Based on the single-parabolic band (SPB) model,[71] the S and σ are usually interwoven, as described by

$$S = \frac{8\pi^2 K_B^2 T}{3e\hbar^2} m^* \left(\frac{\pi}{3n}\right)^{2/3} \tag{5}$$

and

$$\sigma = \frac{ne^2\tau}{m^*} \tag{6}$$

where n in the carrier concentration. The existence of occupied Te−Te π^*, π, and σ bondings significantly enhanced the p-type electrical conductivity, which is comparable to the 2D α-Te (uniform covalent bonding)[50] and much higher than that of the 2D CdTe. The high electrical concentration in p-type $CdTe_2$ also induces high electronic thermal conductivity. As shown in Figure S5, the total thermal conductivity of p-type $CdTe_2$ at 300 K is much higher than that of CdTe and n-type $CdTe_2$. However, the p-type $CdTe_2$ still exhibits high S, comparable to that of CdTe. Such an abnormal character is dominantly contributed by the highly degenerated band structure as discussed above. On the basis of the calculated S and σ, we calculated the PF ($S^2\sigma$) for CdTe and $CdTe_2$. The maximum PFs at 300 K are 2.8 and 1.5 mW m^{-1}K^{-2} for p- and n-types, respectively of CdTe. The superior σ and S lead to the largest PF in the p-type $CdTe_2$, which is 38.3 mW m^{-1}K^{-2}.

Figure of Merit. On the basis of the above-mentioned results, we calculated the figure of merit $zT = S^2\sigma T/(\kappa_e + \kappa_L)$. Figure 6a,b shows the results for 2D CdTe and $CdTe_2$ at 300, 500, and 700 K. The zT values are strongly correlated with temperature and carrier concentration. For CdTe, the zT_{max} is 0.69 for the p-type and 0.60 for the n-type system at 300 K. The high power factor and low κ_L give rise to a substantially

https://doi.org/10.1021/acsaem.2c01176
ACS Appl. Energy Mater. 2022, 5, 9549−9558

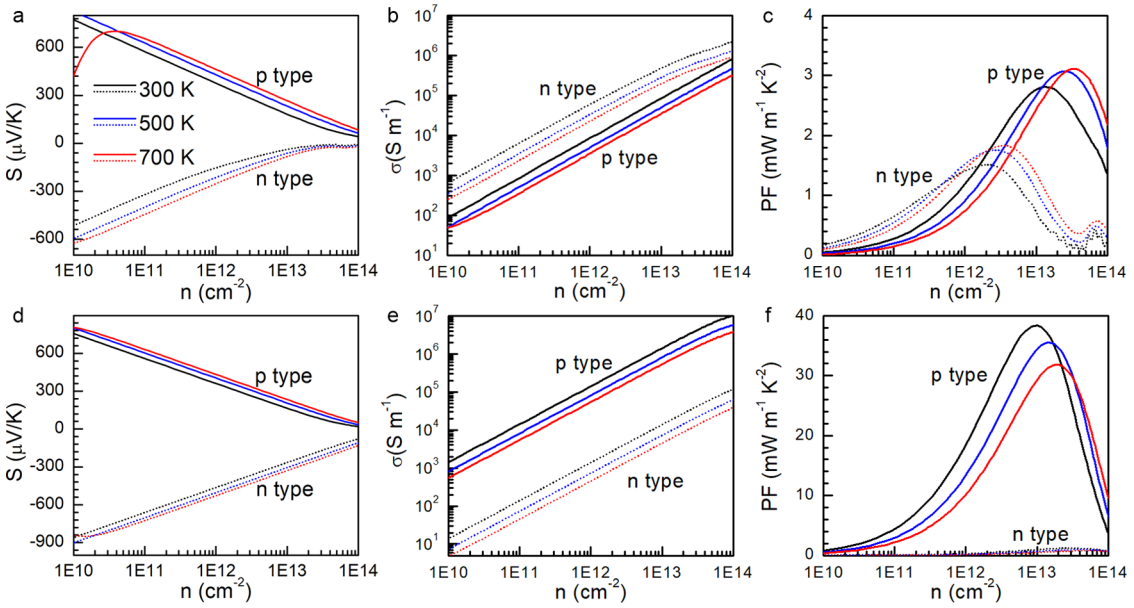

Figure 5. Calculated Seebeck coefficient, electrical conductivity, and power factor ($S^2\sigma$) of CdTe (a–c) and $CdTe_2$ (d–f) monolayers, respectively, as a function of the carrier concentration along the *a* or *b* axis at 300, 500, and 700 K.

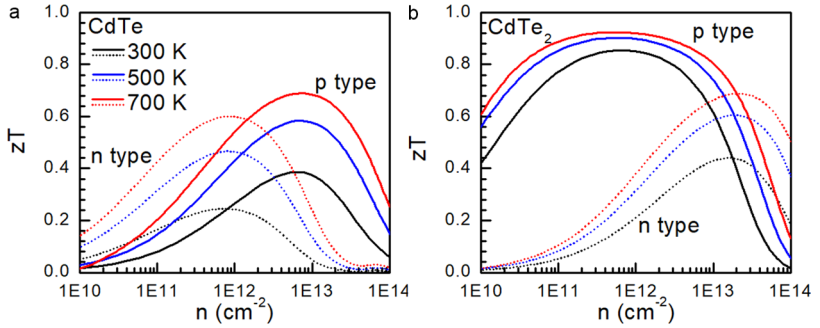

Figure 6. Calculated n- and p-type figure of merit (zT) of CdTe (a) and $CdTe_2$ (b) as a function of carrier concentration along the *a* or *b* axis at 300, 500, and 700 K.

larger zT_{max} of p-type $CdTe_2$, i.e., 0.85, 0.90, and 0.92 at 300, 500, and 700 K, respectively, which is higher than that of α-Te (0.54 at 300 K)[50] and H-$PdTe_2$ (0.8 at 300 K).[32] The high zT_{max} suggests that $CdTe_2$ is a promising room temperature thermometric material. Moreover, the zT_{max} for p-type $CdTe_2$ is almost unchanged in a wide range of carrier concentrations ($3 \times 10^{10} - 1 \times 10^{13}$ cm^{-2}). Such a character is important, since the high band gaps of CdTe and $CdTe_2$ indicate that a sufficient carrier concentration is difficult to achieve. The low thermal conductivity also renders $CdTe_2$ a promising candidate in low-thermal conductivity applications.

CONCLUSIONS

In conclusion, through the extensive structural search method, we explored the potential 2D CdTe compounds. The most stable 2D CdTe and $CdTe_2$ crystallize in the space groups $P\bar{3}m1$ and $P\bar{4}2_1m$, respectively. Both the 2D CdTe and $CdTe_2$ show low formation enthalpies and excellent dynamic stability, making them promising for synthesis. In CdTe, all the atoms are coupled through ionic bonding. $CdTe_2$ exhibits strong bonding heterogeneity, originating from the weak Cd–Te ionic bonding and strong Te–Te covalent bonding. The quasi-localized phonon branches, low group velocities of the acoustic modes, and high lattice anharmonicity in $CdTe_2$ induced a low κ_L of 0.33 Wm^{-1} K^{-1} at 300 K. The occupied π^*_{5p}, π_{5p}, and σ_{5p} bondings in Te–Te pairs facilitate the electronic conductivity and enhance the Seebeck coefficient of p-type $CdTe_2$. The low lattice thermal conductivity and high electronic conductivity endow $CdTe_2$ with a considerably larger maximum zT~0.85 for the p-type system, making it a promising room temperature thermometric material.

ASSOCIATED CONTENT

Supporting Information

The Supporting Information is available free of charge at https://pubs.acs.org/doi/10.1021/acsaem.2c01176.

κ_L convergence test, crystal structure of metastable 2D CdTe, $CdTe_2$, and $CdTe_3$, lattice parameters and atomic position of most stable CdTe and $CdTe_2$, group velocity, and mode Gruneisen parameter for CdTe and $CdTe_2$ at 300 K (PDF)

AUTHOR INFORMATION

Corresponding Author

Zhuangfei Zhang – *Key Laboratory of Material Physics of Ministry of Education, School of Physics and Microelectronics, Zhengzhou University, Zhengzhou 450052, China;*

https://doi.org/10.1021/acsaem.2c01176
ACS Appl. Energy Mater. 2022, 5, 9549–9558

orcid.org/0000-0002-1148-0455; Email: zhangzf@zzu.edu.cn

Authors

Biao Wan − *Key Laboratory of Material Physics of Ministry of Education, School of Physics and Microelectronics, Zhengzhou University, Zhengzhou 450052, China;* orcid.org/0000-0003-4441-9340

Zhibin Gao − *State Key Laboratory for Mechanical Behavior of Materials, Xi'an Jiaotong University, Xi'an, Shanxi 710049, China*

Xiaochen Huang − *Key Laboratory of Material Physics of Ministry of Education, School of Physics and Microelectronics, Zhengzhou University, Zhengzhou 450052, China*

Yuqian Yang − *Department of Physics, Hebei Normal University of Science & Technology, Qinhuangdao 066004, China*

Liangchao Chen − *Key Laboratory of Material Physics of Ministry of Education, School of Physics and Microelectronics, Zhengzhou University, Zhengzhou 450052, China*

Qianqian Wang − *Key Laboratory of Material Physics of Ministry of Education, School of Physics and Microelectronics, Zhengzhou University, Zhengzhou 450052, China*

Chao Fang − *Key Laboratory of Material Physics of Ministry of Education, School of Physics and Microelectronics, Zhengzhou University, Zhengzhou 450052, China;* orcid.org/0000-0001-7322-1566

Weixia Shen − *Key Laboratory of Material Physics of Ministry of Education, School of Physics and Microelectronics, Zhengzhou University, Zhengzhou 450052, China*

Yuewen Zhang − *Key Laboratory of Material Physics of Ministry of Education, School of Physics and Microelectronics, Zhengzhou University, Zhengzhou 450052, China;* orcid.org/0000-0003-3362-5085

Hongan Ma − *State Key Laboratory of Superhard Materials, College of Physics, Jilin University, Changchun 130012, China*

Huiyang Gou − *Center for High Pressure Science and Technology Advanced Research, Beijing 100094, China;* orcid.org/0000-0002-2612-4314

Xiaopeng Jia − *Key Laboratory of Material Physics of Ministry of Education, School of Physics and Microelectronics, Zhengzhou University, Zhengzhou 450052, China*

Complete contact information is available at: https://pubs.acs.org/10.1021/acsaem.2c01176

Notes

The authors declare no competing financial interest.

■ ACKNOWLEDGMENTS

This work was supported by the National Natural Science Foundation of China (No. 11704340, 11804305, 12104408, 12004342, 12104356, and 12004341), China the Postdoctoral Science Foundation (No. 2021M702956), and the Scientific and Technology project in Henan Province (No. 202102210198). Yuqian Yang was supported by the Natural Science Foundation of Hebei Province of China (No. E2021407006).

■ REFERENCES

(1) Snyder, G. J.; Toberer, E. S. Complex Thermoelectric Materials. *Nat. Mater.* **2008**, *7*, 105−114.

(2) Yang, L.; Chen, Z.-G.; Dargusch, M. S.; Zou, J. High Performance Thermoelectric Materials: Progress and Their Applications. *Adv. Energy Mater.* **2018**, *8*, No. 1701797.

(3) Zeier, W. G.; Zevalkink, A.; Gibbs, Z. M.; Hautier, G.; Kanatzidis, M. G.; Snyder, G. J. Thinking Like a Chemist: Intuition in Thermoelectric Materials. *Angew. Chem., Int. Ed.* **2016**, *55*, 6826−6841.

(4) Tan, G.; Zhao, L.-D.; Kanatzidis, M. G. Rationally Designing High-Performance Bulk Thermoelectric Materials. *Chem. Rev.* **2016**, *116*, 12123−12149.

(5) Alsaleh, N. M.; Shoko, E.; Schwingenschlögl, U. Pressure-Induced Conduction Band Convergence in the Thermoelectric Ternary Chalcogenide $CuBiS_2$. *Phys. Chem. Chem. Phys.* **2019**, *21*, 662−673.

(6) Ji, W.; Shi, X.-L.; Liu, W.-D.; Yuan, H.; Zheng, K.; Wan, B.; Shen, W.; Zhang, Z.; Fang, C.; Wang, Q.; Chen, L.; Zhang, Y.; Jia, X.; Chen, Z.-G. Boosting the Thermoelectric Performance of N-Type Bi_2S_3 by Hierarchical Structure Manipulation and Carrier Density Optimization. *Nano Energy* **2021**, *87*, No. 106171.

(7) Garmroudi, F.; Riss, A.; Parzer, M.; Reumann, N.; Müller, H.; Bauer, E.; Khmelevskyi, S.; Podloucky, R.; Mori, T.; Tobita, K.; Katsura, Y.; Kimura, K. Boosting the Thermoelectric Performance of Fe_2VAl-type Heusler Compounds by Band Engineering. *Phys. Rev. B* **2021**, *103*, No. 085202.

(8) Isaacs, E. B.; Wolverton, C. Inverse Band Structure Design via Materials Database Screening: Application to Square Planar Thermoelectrics. *Chem. Mater.* **2018**, *30*, 1540−1546.

(9) Bilc, D. I.; Hautier, G.; Waroquiers, D.; Rignanese, G.-M.; Ghosez, P. Low-Dimensional Transport and Large Thermoelectric Power Factors in Bulk Semiconductors by Band Engineering of Highly Directional Electronic States. *Phys. Rev. Lett.* **2015**, *114*, No. 136601.

(10) Tang, Y.; Gibbs, Z. M.; Agapito, L. A.; Li, G.; Kim, H.-S.; Nardelli, M. B.; Curtarolo, S.; Snyder, G. J. Convergence of Multi-Valley Bands as the Electronic Origin of High Thermoelectric Performance in $CoSb_3$ Skutterudites. *Nat. Mater.* **2015**, *14*, 1223−1228.

(11) Zianni, X. Thermoelectric Metamaterials: Nano-Waveguides for Thermoelectric Energy Conversion and Heat Management at the Nanoscale. *Adv. Electron. Mater.* **2021**, *7*, No. 2100176.

(12) Biswas, K.; He, J.; Blum, I. D.; Wu, C.-I.; Hogan, T. P.; Seidman, D. N.; Dravid, V. P.; Kanatzidis, M. G. High-Performance Bulk Thermoelectrics with All-Scale Hierarchical Architectures. *Nature* **2012**, *489*, 414−418.

(13) Ichinose, Y.; Matsubara, M.; Yomogida, Y.; Yoshida, A.; Ueji, K.; Kanahashi, K.; Pu, J.; Takenobu, T.; Yamamoto, T.; Yanagi, K. One-Dimensionality of Thermoelectric Properties of Semiconducting Nanomaterials. *Phys. Rev. Mater.* **2021**, *5*, No. 025404.

(14) Pal, K.; He, J.; Wolverton, C. Bonding Hierarchy Gives Rise to High Thermoelectric Performance in Layered Zintl Compound $BaAu_2P_4$. *Chem. Mater.* **2018**, *30*, 7760−7768.

(15) Samanta, M.; Pal, K.; Pal, P.; Waghmare, U. V.; Biswas, K. Localized Vibrations of Bi Bilayer Leading to Ultralow Lattice Thermal Conductivity and High Thermoelectric Performance in Weak Topological Insulator N-Type BiSe. *J. Am. Chem. Soc.* **2018**, *140*, 5866−5872.

(16) Lee, S.; Esfarjani, K.; Luo, T.; Zhou, J.; Tian, Z.; Chen, G. Resonant Bonding Leads to Low Lattice Thermal Conductivity. *Nat. Commun.* **2014**, *5*, No. 3525.

(17) Zhang, Y.; Skoug, E.; Cain, J.; Ozoliņš, V.; Morelli, D.; Wolverton, C. First-Principles Description of Anomalously Low Lattice Thermal Conductivity in Thermoelectric Cu-Sb-Se Ternary Semiconductors. *Phys. Rev. B* **2012**, *85*, No. 054306.

(18) Lin, H.; Tan, G.; Shen, J.-N.; Hao, S.; Wu, L.-M.; Calta, N.; Malliakas, C.; Wang, S.; Uher, C.; Wolverton, C.; Kanatzidis, M. G. Concerted Rattling in $CsAg_5Te_3$ Leading to Ultralow Thermal Conductivity and High Thermoelectric Performance. *Angew. Chem., Int. Ed.* **2016**, *55*, 11431−11436.

(19) Pal, K.; Xia, Y.; He, J.; Wolverton, C. High Thermoelectric Performance in $BaAgYTe_3$ via Low Lattice Thermal Conductivity Induced by Bonding Heterogeneity. *Phys. Rev. Mater.* **2019**, *3*, No. 085402.
(20) Dresselhaus, M. S.; Chen, G.; Tang, M. Y.; Yang, R. G.; Lee, H.; Wang, D. Z.; Ren, Z. F.; Fleurial, J.-P.; Gogna, P. New Directions for Low-Dimensional Thermoelectric Materials. *Adv. Mater.* **2007**, *19*, 1043−1053.
(21) Lan, Y.-S.; Chen, X.-R.; Hu, C.-E.; Cheng, Y.; Chen, Q.-F. Penta-PdX_2 (X = S, Se, Te) Monolayers: Promising Anisotropic Thermoelectric Materials. *J. Mater. Chem. A* **2019**, *7*, 11134−11142.
(22) Tao, W.-L.; Zhao, Y.-Q.; Zeng, Z.-Y.; Chen, X.-R.; Geng, H.-Y. Anisotropic Thermoelectric Materials: Pentagonal PtM_2 (M = S, Se, Te). *ACS Appl. Mater. Interfaces* **2021**, *13*, 8700−8709.
(23) Sun, Z.; Yuan, K.; Chang, Z.; Bi, S.; Zhang, X.; Tang, D. Ultra-Low Thermal Conductivity and High Thermoelectric Performance of Two-Dimensional Triphosphides (InP_3, GaP_3, SbP_3 and SnP_3): A Comprehensive First-Principles Study. *Nanoscale* **2020**, *12*, 3330−3342.
(24) Ouyang, T.; Jiang, E.; Tang, C.; Li, J.; He, C.; Zhong, J. Thermal and Thermoelectric Properties of Monolayer Indium Triphosphide (InP_3): A First-Principles Study. *J. Mater. Chem. A* **2018**, *6*, 21532−21541.
(25) Yu, J.; Li, T.; Nie, G.; Zhang, B.-P.; Sun, Q. Ultralow Lattice Thermal Conductivity Induced High Thermoelectric Performance in the δ-Cu_2S Monolayer. *Nanoscale* **2019**, *11*, 10306−10313.
(26) Sharma, S.; Shafique, A.; Schwingenschlögl, U. Monolayer Ag_2S: Ultralow Lattice Thermal Conductivity and Excellent Thermoelectric Performance. *ACS Appl. Energy Mater.* **2020**, *3*, 10147−10153.
(27) Wang, C.; Wei, S.; Gao, G. Theoretical Investigation of Metal-Shrouded Tl_2O Monolayers: Pudding-Mold-Type Band Structure and Thermoelectric Performance. *ACS Appl. Nano Mater.* **2019**, *2*, 4061−4066.
(28) Chen, X.; Wang, D.; Liu, X.; Li, L.; Sanyal, B. Two-Dimensional Square-A_2B (A = Cu, Ag, Au, and B = S, Se): Auxetic Semiconductors with High Carrier Mobilities and Unusually Low Lattice Thermal Conductivities. *J. Phys. Chem. Lett.* **2020**, *11*, 2925−2933.
(29) Hu, Z.-Y.; Li, K.-Y.; Lu, Y.; Huang, Y.; Shao, X.-H. High Thermoelectric Performances of Monolayer SnSe Allotropes. *Nanoscale* **2017**, *9*, 16093−16100.
(30) Sun, Y.; Li, Y.; Li, T.; Biswas, K.; Patanè, A.; Zhang, L. New Polymorphs of 2D Indium Selenide with Enhanced Electronic Properties. *Adv. Funct. Mater.* **2020**, *30*, No. 2001920.
(31) Liu, C.; Lian, C.-S.; Liao, M.-H.; Wang, Y.; Zhong, Y.; Ding, C.; Li, W.; Song, C.-L.; He, K.; Ma, X.-C.; Duan, W.; Zhang, D.; Xu, Y.; Wang, L.; Xue, Q.-K. Two-Dimensional Superconductivity and Topological States in $PdTe_2$ Thin Films. *Phys. Rev. Mater.* **2018**, *2*, No. 094001.
(32) Marfoua, B.; Hong, J. High Thermoelectric Performance in Hexagonal 2D $PdTe_2$ Monolayer at Room Temperature. *ACS Appl. Mater. Interfaces* **2019**, *11*, 38819−38827.
(33) Li, M.-S.; Chen, K.-X.; Mo, D.-C.; Lyu, S.-S. Predicted High Thermoelectric Performance in a Two-Dimensional Indium Telluride Monolayer and Its Dependence on Strain. *Phys. Chem. Chem. Phys.* **2019**, *21*, 24695−24701.
(34) Xiong, F.; Tan, H. B.; Xia, C.; Chen, Y. Strain and Doping in Two-Dimensional SnTe Nanosheets: Implications for Thermoelectric Conversion. *ACS Appl. Nano Mater.* **2020**, *3*, 114−119.
(35) Zhang, K.-C.; Li, Y.-F.; Liu, Y.; Zhu, Y. First-Principles Study on the Anisotropic Transport of Electrons and Phonons in Monolayer and Bulk GaTe: A Comparative Study. *Phys. Chem. Chem. Phys.* **2020**, *22*, 15270−15280.
(36) Iyikanat, F.; Akbali, B.; Kang, J.; Senger, R. T.; Selamet, Y.; Sahin, H. Stable Ultra-Thin CdTe Crystal: A Robust Direct Gap Semiconductor. *J. Phys.: Condens. Matter* **2017**, *29*, No. 485302.
(37) Rousset, J.; Olsson, P.; McCandless, B.; Lincot, D. Structure and Optoelectronics of Electrodeposited Cadmium Ditelluride ($CdTe_2$). *Chem. Mater.* **2008**, *20*, 6550−6555.
(38) Britt, J.; Ferekides, C. Thin-film CdS/CdTe Solar Cell with 15.8% Efficiency. *Appl. Phys. Lett.* **1993**, *62*, 2851−2852.
(39) Unsal, E.; Senger, R. T.; Sahin, H. Stable Monolayer α-Phase of CdTe: Strain-Dependent Properties. *J. Mater. Chem. C* **2017**, *5*, 12249−12255.
(40) Naseri, M.; Hoat, D. M.; Rivas-Silva, J. F.; Cocoletzi, G. H. Electronic Structure, Optical and Thermoelectric Properties of Cadmium Chalcogenides Monolayers. *Optik* **2020**, *210*, No. 164567.
(41) Kolobov, A. V.; Kuznetsov, V. G.; Fons, P.; Saito, Y.; Elets, D. I.; Hyot, B. Polymorphism of CdTe in the Few-Monolayer Limit. *Phys. Status Solidi RRL* **2021**, *15*, No. 2100358.
(42) Wang, Y.; Lv, J.; Zhu, L.; Ma, Y. CALYPSO: A Method for Crystal Structure Prediction. *Comput. Phys. Commun.* **2012**, *183*, 2063−2070.
(43) Wang, Y.; Lv, J.; Zhu, L.; Ma, Y. Crystal Structure Prediction via Particle-Swarm Optimization. *Phys. Rev. B* **2010**, *82*, No. 094116.
(44) Cai, X.; Chen, Y.; Sun, B.; Chen, J.; Wang, H.; Ni, Y.; Tao, L.; Wang, H.; Zhu, S.; Li, X.; Wang, Y.; Lv, J.; Feng, X.; Redfern, S. A. T.; Chen, Z. Two-Dimensional Blue-AsP Monolayers with Tunable Direct Band Gap and Ultrahigh Carrier Mobility Show Promising High-Performance Photovoltaic Properties. *Nanoscale* **2019**, *11*, 8260−8269.
(45) Wan, B.; Xu, S.; Yuan, X.; Tang, H.; Huang, D.; Zhou, W.; Wu, L.; Zhang, J.; Gou, H. Diversities of Stoichiometry and Electrical Conductivity in Sodium Sulfides. *J. Mater. Chem. A* **2019**, *7*, 16472−16478.
(46) Kresse, G.; Furthmüller, J. Efficient Iterative Schemes for Ab Initio Total-Energy Calculations Using a Plane-Wave Basis Set. *Phys. Rev. B* **1996**, *54*, 11169−11186.
(47) Blöchl, P. E. Projector Augmented-Wave Method. *Phys. Rev. B* **1994**, *50*, 17953−17979.
(48) Perdew, J. P.; Burke, K.; Ernzerhof, M. Generalized Gradient Approximation Made Simple. *Phys. Rev. Lett.* **1996**, *77*, 3865−3868.
(49) Huang, X.; Guan, J.; Lin, Z.; Liu, B.; Xing, S.; Wang, W.; Guo, J. Epitaxial Growth and Band Structure of Te Film on Graphene. *Nano Lett.* **2017**, *17*, 4619−4623.
(50) Gao, Z.; Liu, G.; Ren, J. High Thermoelectric Performance in Two-Dimensional Tellurium: An Ab Initio Study. *ACS Appl. Mater. Interfaces* **2018**, *10*, 40702−40709.
(51) Krukau, A. V.; Vydrov, O. A.; Izmaylov, A. F.; Scuseria, G. E. Influence of the Exchange Screening Parameter on the Performance of Screened Hybrid Functionals. *J. Chem. Phys.* **2006**, *125*, No. 224106.
(52) Nosé, S. A Unified Formulation of the Constant Temperature Molecular Dynamics Methods. *J. Chem. Phys.* **1984**, *81*, 511−519.
(53) Deringer, V. L.; Tchougréeff, A. L.; Dronskowski, R. Crystal Orbital Hamilton Population (COHP) Analysis As Projected from Plane-Wave Basis Sets. *J. Phys. Chem. A* **2011**, *115*, 5461−5466.
(54) Madsen, G. K. H.; Singh, D. J. BoltzTraP. A Code for Calculating Band-Structure Dependent Quantities. *Comput. Phys. Commun.* **2006**, *175*, 67−71.
(55) Chen, M. X.; Podloucky, R. Electronic Thermal Conductivity as Derived by Density Functional Theory. *Phys. Rev. B* **2013**, *88*, No. 045134.
(56) Li, W.; Carrete, J.; A Katcho, N.; Mingo, N. ShengBTE: A Solver of the Boltzmann Transport Equation for Phonons. *Comput. Phys. Commun.* **2014**, *185*, 1747−1758.
(57) Togo, A.; Tanaka, I. First Principles Phonon Calculations in Materials Science. *Scr. Mater.* **2015**, *108*, 1−5.
(58) Savin, A.; Nesper, R.; Wengert, S.; Fassler, T. F. ELF: The Electron Localization Function. *Angew. Chem., Int. Ed.* **1997**, *36*, 1808−1832.
(59) Chang, Y. H. R.; Jiang, J.; Khong, H. Y.; Saad, I.; Chai, S. S.; Mahat, M. M.; Tao, S. Stretchable AgX (X = Se, Te) for Efficient Thermoelectrics and Photovoltaics. *ACS Appl. Mater. Interfaces* **2021**, *13*, 25121−25136.
(60) Sun, Y.; Shuai, Z.; Wang, D. Lattice Thermal Conductivity of Monolayer AsP from First-Principles Molecular Dynamics. *Phys. Chem. Chem. Phys.* **2018**, *20*, 14024−14030.

https://doi.org/10.1021/acsaem.2c01176
ACS Appl. Energy Mater. 2022, 5, 9549−9558

(61) Lad, K. N.; Pratap, A. Velocity Autocorrelation Function for Simple Liquids and Its Application to Liquid Metals and Alloys. *Phys. Rev. E* **2004**, *70*, No. 051201.
(62) Lai, W.; Wang, Y.; Morelli, D. T.; Lu, X. From Bonding Asymmetry to Anharmonic Rattling in $Cu_{12}Sb_4S_{13}$ Tetrahedrites: When Lone-Pair Electrons Are Not So Lonely. *Adv. Funct. Mater.* **2015**, *25*, 3648−3657.
(63) Mukherjee, M.; Singh, A. K. Strong Chemical Bond Hierarchy Leading to Exceptionally High Thermoelectric Figure of Merit in Oxychalcogenide AgBiTeO. *ACS Appl. Mater. Interfaces* **2020**, *12*, 8280−8287.
(64) Meng, Q.-L.; Kong, S.; Huang, Z.; Zhu, Y.; Liu, H.-C.; Lu, X.; Jiang, P.; Bao, X. Simultaneous Enhancement in the Power Factor and Thermoelectric Performance of Copper Sulfide by In_2S_3 Doping. *J. Mater. Chem. A* **2016**, *4*, 12624−12629.
(65) Balandin, A. A. Thermal Properties of Graphene and Nanostructured Carbon Materials. *Nat. Mater.* **2011**, *10*, 569−581.
(66) Takagi, S.; Toriumi, A.; Iwase, M.; Tango, H. On the Universality of Inversion Layer Mobility in Si MOSFET's: Part I-Effects of Substrate Impurity Concentration. *IEEE Trans. Electron Devices* **1994**, *41*, 2357−2362.
(67) Diznab, M. R.; Maleki, I.; Vaez Allaei, S. M.; Xia, Y.; Naghavi, S. S. Achieving an Ultrahigh Power Factor in Sb_2Te_2Se Monolayers via Valence Band Convergence. *ACS Appl. Mater. Interfaces* **2019**, *11*, 46688−46695.
(68) Qiao, J.; Kong, X.; Hu, Z.-X.; Yang, F.; Ji, W. High-Mobility Transport Anisotropy and Linear Dichroism in Few-Layer Black Phosphorus. *Nat. Commun.* **2014**, *5*, No. 4475.
(69) Wang, C.; Zheng, C.; Gao, G. Bulk and Monolayer ZrS_3 as Promising Anisotropic Thermoelectric Materials: A Comparative Study. *J. Phys. Chem. C* **2020**, *124*, 6536−6543.
(70) Gao, Z.; Zhu, T.; Sun, K.; Wang, J.-S. Highly Anisotropic Thermoelectric Properties of Two-Dimensional As_2Te_3. *ACS Appl. Electron. Mater.* **2021**, *3*, 1610−1620.
(71) Heremans, J. P.; Jovovic, V.; Toberer, E. S.; Saramat, Ali.; Kurosaki, K.; Charoenphakdee, A.; Yamanaka, S.; Snyder, G. J. Enhancement of Thermoelectric Efficiency in PbTe by Distortion of the Electronic Density of States. *Science* **2008**, *321*, 554−557.

https://doi.org/10.1021/acsaem.2c01176
ACS Appl. Energy Mater. 2022, 5, 9549−9558